**Article:**
Dixit, A., Jain, V., Smith, M. et al. (2026) Tracking mass-wasting sediments in the large BrahmaputraRiver system. Earth Surface Processes and Landforms, 51 (5). e70297. ISSN: 0197-9337

https://doi.org/10.1002/esp.70297

# Tracking Mass-Wasting Sediments in the Large Brahmaputra River System


**Abstract**

The impact of mass-wasting events on river systems is typically studied in the immediate aftermath and within close proximity to the source area. However, basin-wide hydro-geomorphic responses in large river systems, beyond the immediate post-disaster context, remain poorly understood. In this study, we examine the Eastern Himalayan Syntaxis in the Brahmaputra basin, where the Sendongpu glacier valley has undergone rapid erosion due to major mass-wasting events in 2017, 2018 and 2021. A nearby large-scale event also occurred in 2000 along the Yigong River. We assess the river's response to these events using satellite-derived water turbidity indices, water surface elevation, sandbar area and flood extent, at the finest temporal and spatial resolution available through Google Earth Engine's database. Our time-series analysis reveals that, following the 2017 event, fine suspended sediment signals can be traced more than 1000 km downstream to the delta, while coarser sediments primarily affect river morphology within approximately 100 km of the mountain front. In this zone, we observed a notable increase in sandbar area and water surface elevation, indicating extensive deposition and channel infilling. Comparison with the 2000 Yigong outburst highlights the differing geomorphic effects of rapid, high-magnitude events versus slower, more sustained sediment inputs. These findings highlight the need to integrate mass-wasting-driven sediment processes into flood risk assessments and hydropower planning in Himalayan river systems, particularly as such landscapes are increasingly subject to both natural and anthropogenic pressures.



Keywords: Sendongpu, Yigong, Brahmaputra, Large rivers, Mass wasting, Google Earth Engine, GLOFs

# 1 Introduction

Mass-wasting events generate large volumes of sediment that can profoundly impact both society and the environment (Carrivick and Tweed, 2016; Taylor et al., 2023; Froude and Petley, 2018; Fidan et al., 2024; Sharma et al., 2023). Their effects are typically twofold: (i) direct impacts, where the large sediment surge damages infrastructure, dams, and settlements (e.g., Shugar et al., 2021; Sattar et al., 2025; Li et al., 2022; Zhang et al., 2023), and (ii) indirect impacts, where the influx of sediment reshapes river corridors, modifies channel morphology, and elevates flood risk (Korup, 2004; Li et al., 2020; Sofia and Nikolopoulos, 2020; Ahrendt et al., 2022; Vázquez-Tarrío et al., 2024).

One of the largest recorded mass-wasting events as a co-seismic landslide occurred after the 1950 Assam earthquake, which released 47000 × $10^6$ $m^3$ of sediment, causing prolonged channel aggradation and widespread flooding along the large Brahmaputra River, lasting for decades (Goswami, 1985; Keefer, 1999). The 2021 Chamoli disaster in the upper Ganga basin, with a volume of 23 × $10^6$ $m^3$, severely damaged hydropower infrastructure (Shugar et al., 2021). More recently, the 2023 Sikkim flood, triggered by the collapse of 14.7 × $10^6$ $m^3$ of frozen moraine into a glacier lake, caused an outburst flood that mobilized 270 × $10^6$ $m^3$ of sediment, devastating infrastructure along the Teesta River (Sattar et al., 2025).

Mass-wasting can be triggered by a range of drivers, including meteorological extremes, earthquakes, wildfires, land use changes, and vegetation disturbances (Yanites et al., 2025; Jones et al., 2021; Kashyap et al., 2025). These events also take multiple forms. In glaciated landscapes, ice–rock avalanches, glacier and landslide outburst floods are common, whereas in tectonically active mountain regions, co-seismic landslides and subsequent outburst events often dominate. Extreme precipitation frequently generates widespread landslides (e.g. Rinaldi et al., 2016), delivering large volumes of sediment to river systems. For the purposes of this study, we broadly define mass-wasting as any event capable of supplying anomalously high sediment loads to the fluvial system, whether or not these sediments are ultimately transported downstream.

Once sediments are released, they enter the fluvial system and are transported downstream over spatial and temporal scales that vary widely depending on hydrometeorological conditions (Graf et al., 2024; Bailey et al., 2025; Gayer et al., 2025; Zhang et al., 2016; Wang et al., 2015), topographical or morphological conditions (Croissant et al., 2017; Dai et al., 2021; Zhang et al., 2016; Wang et al., 2015), grain size of the deposits (Fordham et al., 2023; Wang et al., 2015; **?**) and connectivity of the hillslope to a fluvial network (Graf et al., 2024; Yanites et al., 2010) . Finer

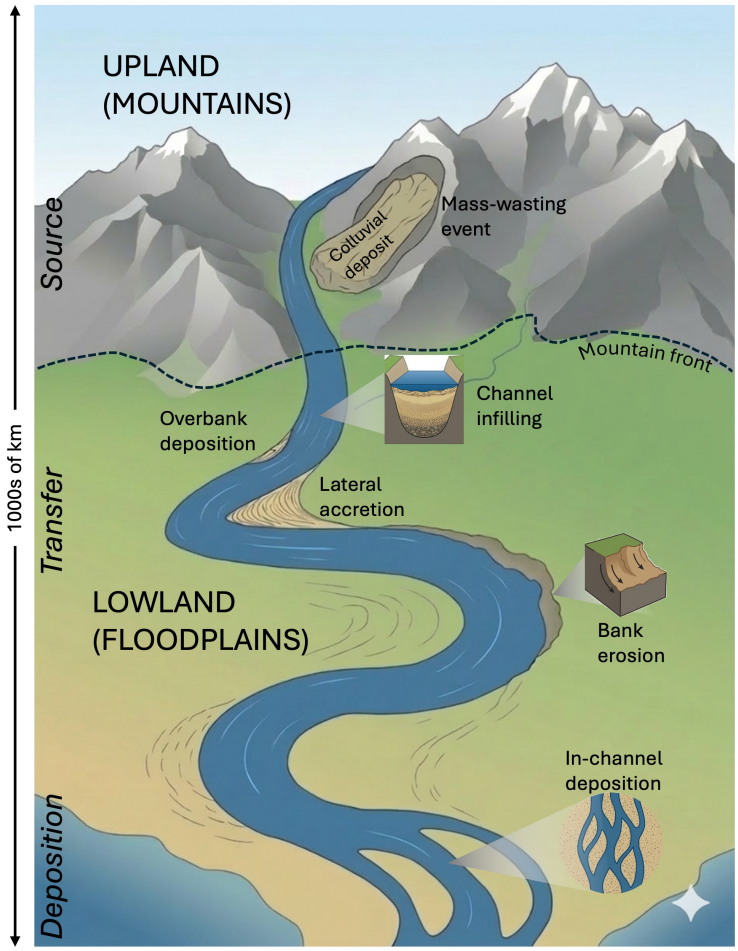


Figure 1: Conceptual diagram showing the transport of mass-wasting sediments and geomorphic alternation in the large river course. Gemini (version 3.00) was used to improve the artistic design of this figure.

sediments in suspension would travel further and faster than the coarse sediments.

The evacuation of mass-wasting sediments typically occurs in two stages: first, the transfer of the material from source (hillslopes or glacier valleys) to river channels; and second, the downstream transport of these sediments once they enter the fluvial network (Croissant et al., 2017). Along this pathway, various geomorphic units act as temporary storage zones (Figure 1), influencing evacuation times. For example, freshly failed sediment may be stored temporarily as colluvial deposits on hillslopes, only to be mobilized later under favorable hydrometeorological conditions (Figure 1). Along the routing pathway, sediment can be stored in overbank deposits, reworked into in-channel bars, or contribute to channel infilling. Tracing *how far* these sediments travel and *how long* they persist is therefore essential for understanding the compounded risks associated with mass-wasting (**?**).

To address the question of time scales (how long) mass-wasting sediments remain in transit, several studies report highly variable timescales ranging from days (Yunus et al., 2025) to years (e.g. Westoby et al., 2023; Croissant et al., 2017; Gayer et al., 2025; Hovius et al., 2011; **?**), and in some cases, decades (e.g. **?**Major et al., 2018; DeLisle et al., 2022; Li et al., 2025; Xiong et al., 2022). However, these studies are mostly limited to a smaller spatial scale (tens to a few hundreds of kilometers). Therefore, an equally important question concerns the spatial extent (how far) of transport. There is a little understanding of geomorphological response (if any) in large river basins (area $> 10^5$ km$^2$, length $> 10^3$ km). Large river basins integrate highly diverse sediment sources, rainfall regimes, and source–sink dynamics (Ashworth and Lewin, 2012; Tandon and Sinha, 2022; Jain et al., 2025). This raises a fundamental question: can localized mass-wasting events, that impact only a very small portion of a basin's area, leave detectable signatures of sediment dispersal and geomorphic change across an entire large river course?

With the advent of cloud-based platforms such as Google Earth Engine, large-scale tracking of mass-wasting signatures is now feasible. Because these events are both short-lived and spatially localized, high spatial and temporal resolution imagery is critical to track the change and response downstream. Available datasets in Google Earth Engine make it possible. While field-based surveys, digital elevation differencing, and numerical models (e.g. in Bennett et al., 2025; Yang et al., 2022) provide volumetric estimates and mechanistic insights of sediment transport, they remain logistically and computationally constrained at basin scales, particularly in large rivers. Instead, remote sensing proxies, such as changes in sandbar area, turbidity, and floodwater extent, offer a consistent, scalable means to assess fluvial response to mass-wasting events across both space and time.

In the Eastern Himalaya, erosion rates are among the highest globally (Kääb and Girod, 2023). Over the last 7–8 years, the Sendongpu glacier alone has eroded approximately $700 \times 10^6$ m$^3$ (1400 Mt) of sediment (Li et al., 2024), nearly three times the Brahmaputra River's annual sediment load of approximately 520 Mt (Milliman and Farnsworth, 2011). Moreover, this region also has a history of megafloods, where outburst floods released discharges and sediment loads several orders of magnitude greater than the present river flow (Lang et al., 2013; Panda et al., 2020; Turzewski et al., 2020). This raises critical questions about the fate of such massive sediment inputs. This study evaluates the *spatial extent* and *persistence* of fluvial response to large-magnitude mass-wasting events in a large river system. We study the mass-wasting events in Sendongpu and the nearby Yigong River, examining the resulting morphological and sedimentary signals in the downstream Large Brahmaputra River across large spatial (1000s of km) and temporal (years) scales, extending

our understanding of processes beyond the immediate, localized post-disaster context.

## 2 Study site and mass-wasting events

The Brahmaputra is a large river basin with an area of about 580,000 $km^2$, and a trunk length of nearly 3,000 km (Figure 2). It originates on the Tibetan Plateau, where it is known as the Yarlung River. After entering the Himalaya, it flows as the Siang through steep topography until reaching the mountain front near Pasighat. Downstream of Pasighat, the river adopts a braided form and flows as the Brahmaputra before draining into the Bay of Bengal. The braided belt width reaches upto 20 km with a braiding index mostly varying between 5 to 15 (Sarma and Acharjee, 2018). The braiding pattern has the presence of sandbars, low-flow channels, chutes, cutoffs and vegetated landforms (Nandi et al., 2022). The Brahmaputra is a sediment-laden river with an annual sediment load of 500 to 1000 $\times 10^6$ tonnes/year (Islam et al., 1999; Galy and France-Lanord, 2001).

A key geomorphic feature of the basin is the Eastern Syntaxis, where the Yarlung River makes a dramatic 180° turn. This region experiences some of the highest erosion rates in the Himalaya (4–21 mm/year) (Lupker et al., 2017; Garzanti et al., 2004; Stewart et al., 2008). In recent decades, it has also been the site of four major mass-wasting events: the 2000 Yigong event and the 2017, 2018, and 2021 Sendongpu events. The Sendongpu valley lies within the Eastern Syntaxis, while the Yigong site, about 50 km away, is located along the Yigong River, a tributary that joins the Yarlung downstream of Sendongpu.

A summary of the mass-wasting events in the Sendongpu and Yigong is provided in SI Table S1. The events are described in detail in the following subsections.

### 2.1 Yigong event (2000)

The 2000 Yigong event is a classic example of a compounding outburst flood. Located approximately 50 km from the site of the Sendongpu events, this disaster began on April 9, 2000, with a massive landslide of approximately $100 \times 10^6$ $m^3$ (Guo et al., 2023; Dong et al., 2024). The landslide evolved into a rock avalanche that blocked the Yigong River, forming a debris dam with an estimated volume of $300 \times 10^6$ $m^3$ (Guo et al., 2023). The blockage created a lake with a volume of approximately 3000 $\times 10^6$ $m^3$ at the time of breaching (Guo et al., 2023). On June 12, 2000, the dam burst suddenly, draining the lake completely and causing extensive damage to downstream areas. In addition, Dong et al. (2024) estimated that an additional $260 \times 10^6$ $m^3$ of sediments were eroded from the valley

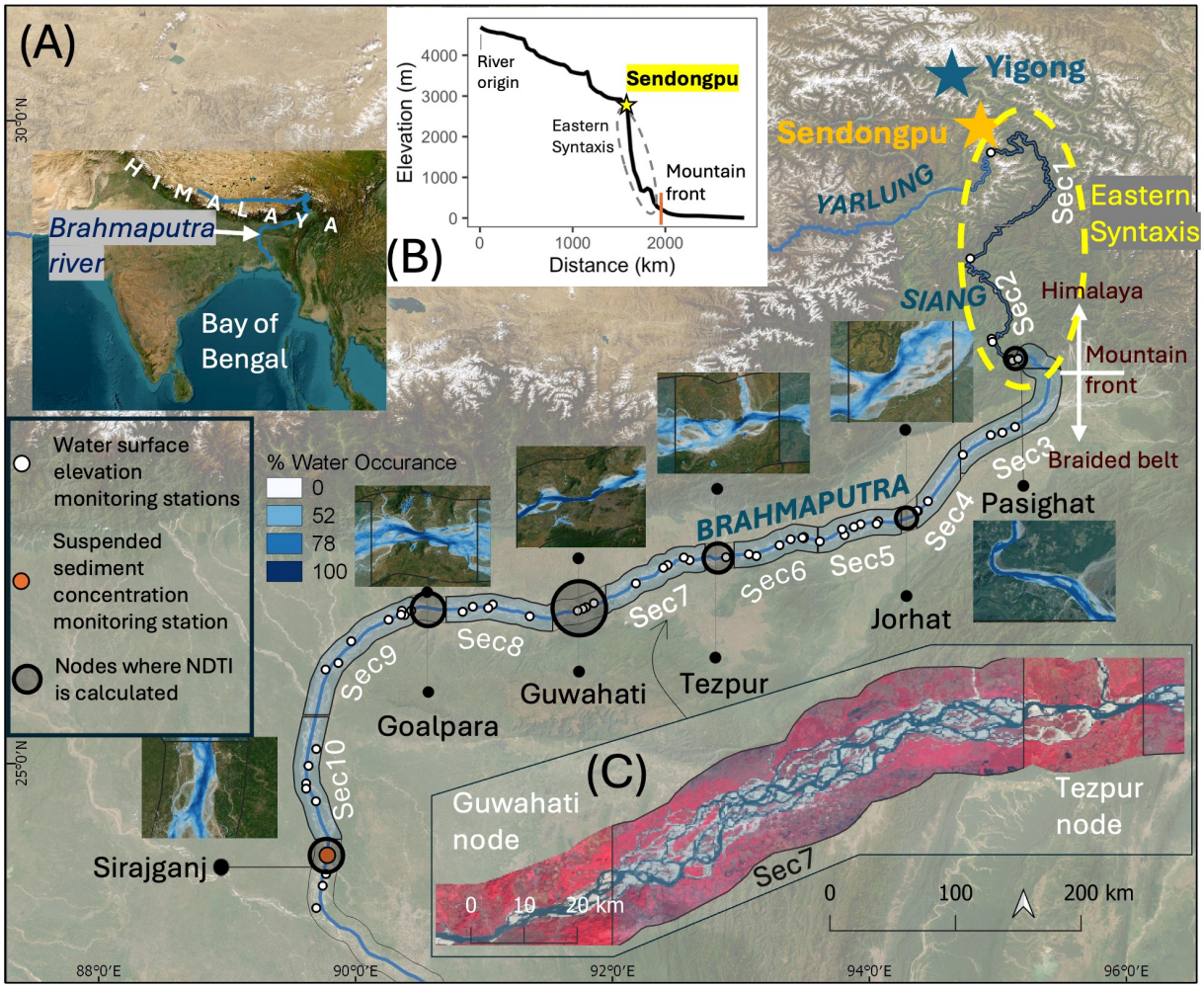


Figure 2: (A) Location of the Yarlung-Siang-Brahmaputra River in the eastern Himalaya, highlighting the studied mass-wasting sites, Yigong and Sendongpu. The river is divided into ten sections (Sec1 to Sec10), each defined by a 20 km buffer around the river centerline. River node locations, derived from the JRC-Global Surface Water dataset (Pekel et al., 2016), are shown on the water occurrence raster and indicate locations of minimal river width and maximum water occurrence probability. Water surface elevation and suspended sediment concentration time series were obtained from the monitoring datasets of Schwatke et al. (DAHITI, 2015) and Dethier et al. (2022), respectively. (B) River long profile along the Yarlung-Siang-Brahmaputra. (C) Below the mountain front, the river transitions to a braided form, shown in false color composite for Sec7. Field photographs of certain locations are shown in SI Figure S1. Basemap source: Esri, Maxar, Earthstar Geographics, and the GIS User Community.

floor and concurrent landslides were triggered due to the outburst as far as 80 km downstream of the outburst flood location.

## 2.2 Sendongpu events (2017-2021)

Sedongpu has a history of mass wasting events (Kääb and Girod, 2023). In this study, we consider three events, one in each of 2017, 2018 and 2021. During 2017, there were ice-rock avalanche and debris flows from 20 Oct 2017 to Jan 2018. The total volume of material that detached from the hillslope during this time was 50 $\times 10^6$ $m^3$. On 18 Nov 2017, a Mw 6.4 earthquake also struck the region (Figure 3). This earthquake triggered 1816 landslides in the upper section of the Siang River (Sec 1 in Figure 2) (Hu et al., 2018, 2019). The average volume of these landslides was estimated at $14 \times 10^6$ $m^3$ (Zhao et al., 2021). Occasionally, the debris deposits blocked the river in this period, which eventually breached or overtopped (Hu et al., 2018; Zhao et al., 2019, 2021).

Following the series of events in 2017, significant changes were observed on the glaciers of the Sendongpu valley (Kääb et al., 2021). Eventually, a large glacier detachment occurred a year later in 2018 (October 17) at the Sendongpu glacier tongue. The glacier detachment mobilized a total of $180 \times 10^6$ $m^3$ of sediment from the glacier tongue. The river blockage caused by these events resulted in the formation of a lake with a volume of approximately $490 \times 10^6$ $m^3$. The debris fan that formed the dam had a crest length of 300 m along the river, a base length of 1.9 km and a height of 79 m (Chen et al., 2020). The dam stored an estimated $35 \times 10^6$ $m^3$ of sediment, accounting for approximately 20% of the total sediment mobilized from the detachment of the glacier tongue (Li et al., 2024).

The 2021 Sendongpu events were among the most intense and significant in the region. On March 22, 2021, a massive ice-rock avalanche occurred, mobilizing approximately $50 \times 10^6$ $m^3$ of material from the eastern flank of the Sendongpu glacier (Kääb and Girod, 2023). Subsequently, between April and September 2021, an additional $279 \times 10^6$ $m^3$ of sediment was mobilized from the glacier tongue area, where similar events had occurred in 2018.

Unlike earlier events, those in 2021 did not cause a significant river blockage, allowing the river to continue flowing uninterrupted. However, the exact quantity of sediment that entered the river and was transported downstream remains unquantified. Nevertheless, studies by Zhao et al. (2022) and Kääb and Girod (2023) suggest far-reaching downstream transport of the mobilized sediments.

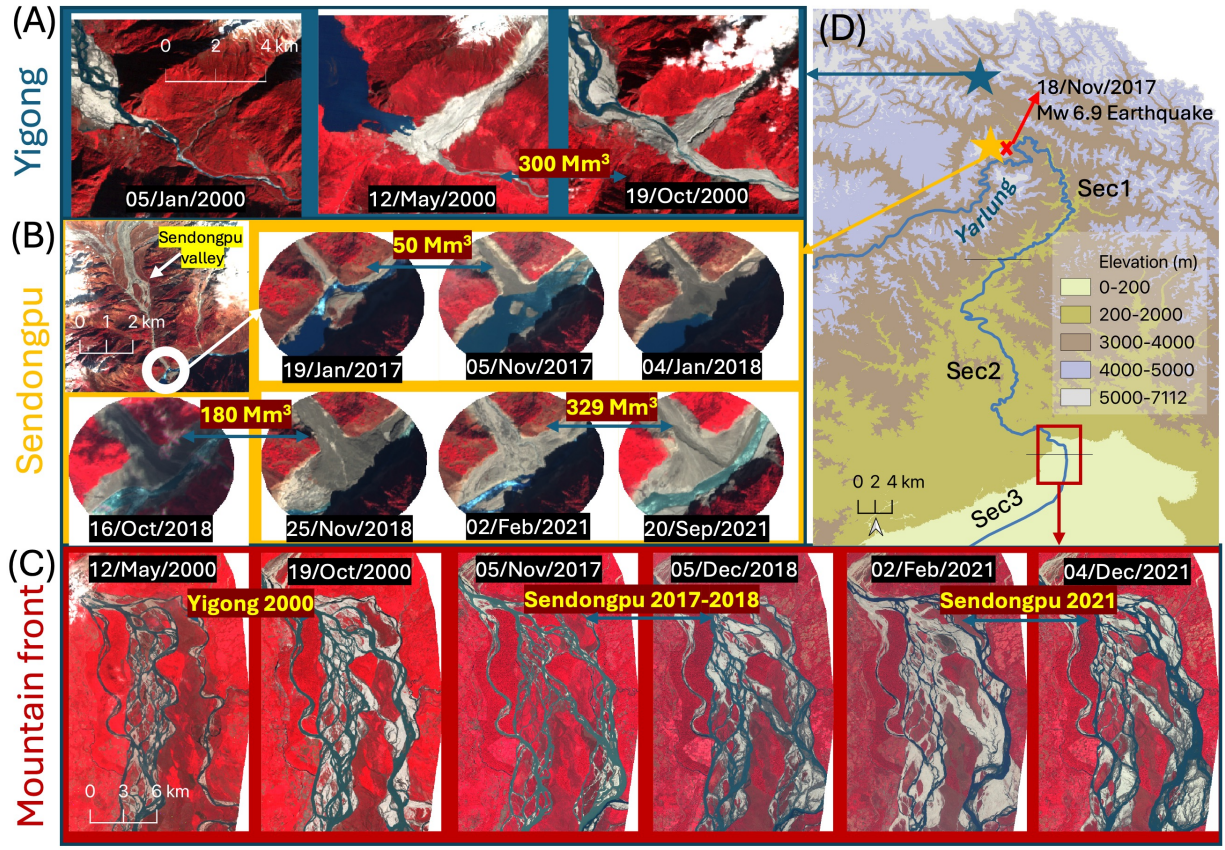


Figure 3: Location of the Yigong (A) and Sendongpu (B) mass-wasting site with the timeline and magnitude of mass-wasting events in 2000, 2017, 2018 and 2021. Sediment volumes generated by these events are shown in yellow. Panel C shows the river planform response downstream of the mountain front (part of Sec3) following the Yigong and Sendongpu events. Panel D shows the elevation map of the study region. All optical satellite images are in false color composite.

Table 1: Summary of the derived dataset and its attributes used in this study.

| Parameter | Source | Spatial Resolution | Spatial Coverage | Temporal Resolution | Temporal Coverage |
|---|---|---|---|---|---|
| **Normalize difference turbidity index** | Landsat5, Landsat8 | 30 m | 6 time series zones along the Brahmaputra | 15 days | 1988-2024 |
| **% Sandbar area** | Dynamic world | 10 m | 10 sections along the Yarlung-Siang-Brahmaputra | 5-10 days | 2017-2024 |
| **Water surface elevation** | DAHITI | - | 59 time series locations along the 1000 km Yarlung-Siang-Brahmaputra | 10-35 days | 2002-2024 |
| **Suspended sediment concentration** | Dethier et al., (2022) | - | 1 time series location in delta | 15 days | 1988-2020 |
| **Optical imagery** | Landsat 7, Sentinel 2 | 30 m, 10 m | Stretch of Yarlung-Siang-Brahmaputra | 5, 15 days | 2000, 2017-2024 |
| **Microwave imagery** | Sentinel 1 | 10 m | Stretch of Yarlung-Siang-Brahmaputra | 12 days | 2017-2024 |
| **Rainfall** | CHIRPS | 5.4 km | Basin of Yarlung-Siang | 5 days | 2000-2024 |

# 3 Data and methods

In this study, multiple proxies were employed to investigate changes in the river planform, water turbidity/suspended sediment concentration and river water surface elevation in relation to mass-wasting events. These parameters were analyzed across the entire Yarlung-Siang-Brahmaputra stretch of approximately 1230 km at the finest spatial (10-30 m) and temporal resolution available (5-30 days). A summary of the datasets used, along with their spatial and temporal resolutions and coverage, is provided in Table 1.

To assess changes following mass-wasting events, we focused on suspended sediment, using the satellite-derived turbidity index as a primary proxy, complemented by suspended sediment concentration data at a single location in Sirajganj from Dethier et al. (2022) (Figure 2). Additionally, we examined changes in the river planform by utilizing the Dynamic World global land use and land cover dataset (Brown et al., 2022). As channel forms are expected to change due to these events, we also analyzed variations in water surface elevation. These changes serve as a proxy for channel infilling, which typically leads to an increase in water surface elevation.

## 3.1 River water turbidity

The Normalized Difference Turbidity Index (NDTI) is a remote sensing-derived index used to measure water turbidity by leveraging the difference in reflectance between specific spectral bands sensitive to sediment concentration in water. The NDTI is calculated using the red and green spectral

bands as:

$$NDTI = \frac{Red - Green}{Red + Green}$$

The resulting NDTI values range from -1 to 1, where higher values indicate greater turbidity (Lacaux et al., 2007). Similarly, the Modified Normalized Difference Water Index (MNDWI) is used to differentiate water pixels from non-water pixels. It is calculated as:

$$MNDWI = \frac{Green - SWIR}{Green + SWIR}$$

where SWIR refers to the shortwave infrared band. MNDWI values range from -1 to 1, with negative values indicating water pixels (Xu, 2006).

To capture turbidity dynamics, the NDTI was calculated at six nodes, namely Pasighat, Jorhat, Tezpur, Guwahati, Goalpara and Sirajganj, along the main trunk of the river (Figure 2). These nodes were selected based on their geomorphic characteristics, where the river exhibits minimum width and predominantly follows a single-channel flow pattern with high water occurrence probabilities (Figure 2 and SI Figures S1b, S1c, S1e). This approach ensured we selected the areas where the water flux was concentrated within a narrow channel, increasing the likelihood of obtaining representative turbidity signatures in the water crossing each cross-section. In contrast, sections with braided channels were excluded due to the difficulty in identifying a representative channel.

The analysis was conducted using Google Earth Engine, a cloud-based geospatial processing platform. Landsat 5 imagery was used to calculate the NDTI for the period 1984–2013 and Landsat 8 imagery was used for 2013–2024. The MNDWI was first applied to all images to delineate water pixels, ensuring that the NDTI calculations were restricted exclusively to water-covered areas. For each of the selected nodes, median NDTI values were computed and aggregated at a daily resolution for cloud-free pixels. Since the median statistic was applied to the NDTI values of all water pixels, no filtering based on pixel count was performed. This approach assumes spatial homogeneity in water turbidity for the small area covered by each node. SI Figure S2 illustrates the pixel count for each image used in the computation of median NDTI values. The mean standard deviation of NDTI values within a single image was approximately 0.03.

## 3.2 Planform analysis

Planform change analysis was conducted by estimating the exposed sandbar area in sections of the braided reach. We utilized the Dynamic World dataset from 2017 to 2024 available in Google Earth Engine. It is a global, high-resolution land cover dataset utilizing deep learning models applied to Sentinel-2 satellite imagery to provide near real-time dynamic classifications of land cover (Brown et al., 2022). It includes nine distinct land cover classes: water, trees, grass, flooded vegetation crops, shrubs, built-up areas, bare ground and snow/ice. The bare class corresponds to the exposed sandbar. We estimated the percent sandbar area in Google Earth Engine for ten sections each of approximately equal length, as shown in Figure 2. Only scenes with the highest pixel count (representing maximum spatial coverage) were selected for further analysis (black points in SI Figure S2B). Scenes with lower pixel counts due to partial coverage and cloud cover were excluded (shown in light gray in SI Figure S2B). Sandbar area proportion was given as:

$$\%\text{Sandbar area} = \text{Bare area pixel count} / \text{Total pixel count}.$$

The Dynamic World dataset has an overall classification accuracy of 73%, with the "bare ground" class achieving an accuracy of approximately 60% (Brown et al., 2022).

## 3.3 Water extent mapping using Synthetic Aperture Radar

To identify the potential effect of mass-wasting events on the flood area, we performed a temporal analysis of the maximum water extent in Sec3 (Figure 2) using Synthetic Aperture Radar (SAR) imagery acquired from the Sentinel-1 satellite on the Google Earth Engine platform. Since the maximum water extent occurs during the monsoon months when significant cloud cover limits the applicability of optical data, application of SAR based analysis gives an opportunity to get insights of flood area during the monsoon months.

The SAR images from Google Earth Engine provide normalized, calibrated and ortho-rectified backscatter coefficients ($\sigma_o$), which were converted to decibels (dB) using the equation $10 \log_{10} \sigma_o$. The backscatter coefficient indicates the proportion of radar energy reflected back to the antenna, influenced by factors such as dielectric constant, surface roughness, topography and local incidence angle. Water has a high dielectric constant, resulting in minimal backscatter compared to land surfaces. Smooth water surfaces produce significantly lower backscatter, whereas rougher surfaces exhibit slightly higher values, assuming other factors remain constant (Campbell and Wynne, 2011; Smith et al., 1996).

The images were obtained in Ground Range Detected mode, using the VH polarization band with a spatial resolution of 30 m. In this analysis, we focused on the VH polarization band, as it is less sensitive to river surface roughness compared to other bands (Dubey and Singh, 2021). To derive the annual maximum water extent, we created a minimum-value composite of the image collection. The minimum-value composite takes the minimum value of each pixel across all the images in the image collection of each year, from January to December, which covers the monsoon months of April to October. This approach assumes that pixels with the lowest backscatter values during the year are most likely water pixels, as inundated areas exhibit minimal radar backscatter. This analysis was undertaken for the 2015 to 2024 period, and include all available SAR images. Ultimately, this yielded ten images of minimum-value composite corresponding to each year, and they, in turn, indicated the maximum water extent most likely corresponding to the monsoon months of each year.

It should be noted that Sentinel-1 has a nominal revisit time of 12 days, with more frequent observations in overlapping swaths. However, since SAR acquisitions are not always synchronous with the true peak of river discharge, the resulting composites may underestimate the absolute flood extent in any given year. Nevertheless, the consistent use of minimum composites across years allows for the detection of relative trends. Thus, while the method may not capture exact peak flood extents, it can effectively reveal persistent, systematic changes in maximum water extent associated with sediment-driven morphological alterations during the monsoon months.

### 3.4 Hydrometric data and other satellite products

We utilized data from the DAHITI (Database for Hydrological Time Series of Inland Waters) platform to analyze changes in water surface elevation along the Brahmaputra River (Schwatke et al., 2015). DAHITI employs satellite altimetry data from multiple missions (e.g., Jason-3 and Sentinel-3) to generate water level time series for inland water bodies. For this study, water surface elevation time series were obtained at 59 locations along the main trunk of the Brahmaputra, spanning from Sendongpu to Sirajganj (Figure 2). The temporal frequency of the observation is 10-35 days. The median error of each of these locations varies from 0.001 m to 0.19 m. To ensure comparability, water surface elevation at each location was normalized to local minimum and maximum values.

For visual inspection of the planform change, we collected optical satellite images from the Sentinel-2: MSI (Multi Spectral Instrument), specifically for the red, green and near-infrared bands, and a time series of suspended sediment concentration was sourced from Dethier et al. (2022) at

the Sirajganj (Figure 2). Rainfall data at a 5-day time interval was provided by the Climate Hazards Group InfraRed Precipitation with Station (CHIRPS) dataset (Funk et al., 2015), and was accessed via GEE platform and an annual composite of mean monsoon rainfall was derived to identify potential extreme meteorological controls on the geomorphological response.

### 3.5 Statistical analysis

To detect the significance of the change in parameters, we performed non-parametric statistical tests due to the lack of normality in the data distributions. Each parameter was categorized into test groups after visual inspection of the long time series. For each parameter, we first applied the Kruskal-Wallis test, a rank-based method, to assess the overall significance of differences across groups (Kruskal and Wallis, 1952). If the Kruskal-Wallis test indicated significant differences ($p < 0.05$), we conducted Dunn's post-hoc test with Bonferroni correction to identify specific pairwise differences (Dunn, 1964). The details of these tests are presented in SI Section SS1 and SI Figures S10, S11.

## 4 Results

### 4.1 Suspended sediment dynamics

Typically, NDTI values during the non-monsoon (October-April) season are low due to low sediment concentration. However, mass-wasting events of 2017 in Sendongpu and co-seismic landslides led to the increase in non-monsoon NDTI values at Pasighat to the levels comparable to those observed during the monsoon months (April-September) (Figures 4A and SI Figure S3). Figure 3C and SI Figure S4 illustrate the river channel near Pasighat with visibly turbid water on November 5, 2017, compared to other times. Local media reports (SANDRP, 2017; Times of India, 2017) indicated turbidity levels as high as 425 NTU on November 27, 2017 in Siang, significantly exceeding the normal range of 12–15 NTU for that time of year.

The 2017-2018 non-monsoon NDTI values were significantly ($p < 0.05$) higher at Pasighat than all other non-monsoon periods as a whole post-2012. Downstream nodes also recorded elevated turbidity during the same period, though the intensity diminished further downstream at Sirajganj ($p = 0.08$). However, post-monsoon suspended sediment concentrations at Sirajganj remained significantly higher ($p < 0.05$) from 2017–2020 compared to the 2013–2016 period (Figure 4B).

Similarly, non-monsoon NDTI values in 2018–2019 remained significantly elevated at Pasighat, Jorhat and Tezpur ($p < 0.05$) but were not statistically significant at Guwahati, Goalpara and Sirajganj, suggesting a gradual attenuation of the sediment signature downstream in later years. During the 2021 monsoon, when much of the sediment from the 2021 mass-wasting events was transported, turbidity levels were significantly ($p < 0.05$) elevated at Pasighat and Jorhat compared to the monsoon period of 2013-2024 as a whole (Figure 4A). Zhao et al. (2022) also mentioned a high amount of turbidity at 200 km downstream of Sendongpu. However, neither the 2018 nor the 2021 events caused turbidity increases as dramatic as those observed after the 2017 event. Additionally, the 2000 Yigong event is distinctly identifiable as an outlier in the suspended sediment concentration records at Sirajganj.

## 4.2 Water surface elevation

Figure 5 illustrates water surface elevation variations in and around Sec3. The normalized water surface elevation for the entire Yarlung-Siang-Brahmaputra stretch is provided in SI Figure S5. Across all sections and nodes, a consistent elevation pattern is observed, except for two data locations in Sec3 (locations 7 and 10 in Figure 5), which exhibit notable variations. These two locations are the only ones within Sec3 with time series data extending beyond 2016. Both show a significant increasing trend ($p < 0.05$, SI Figure S10) in water surface elevation, especially during non-monsoon months (Oct-Mar). The temporal alignment of these changes with upstream mass-wasting events (marked by red stars in Figure 5) is particularly notable.

The water surface elevation increases during non-monsoon months in Sec3 suggest channel infilling as the likely mechanism. While monsoonal water surface elevation fluctuate annually, they remain constrained by an upper limit as excess water spills onto the floodplain/sandbars. In contrast, non-monsoon low water surface elevation is more sensitive to external controls as they fluctuate within the channel boundary.

Sec3 extends approximately 100 km downstream of the mountain front (near location 6 in Figure 5), beyond which, in Sec4 and Sec2, no significant ($p > 0.05$) elevation changes are detected. This indicates that planform changes are largely confined to the first 100 km downstream of the mountain front (location 6 in Figure 5).

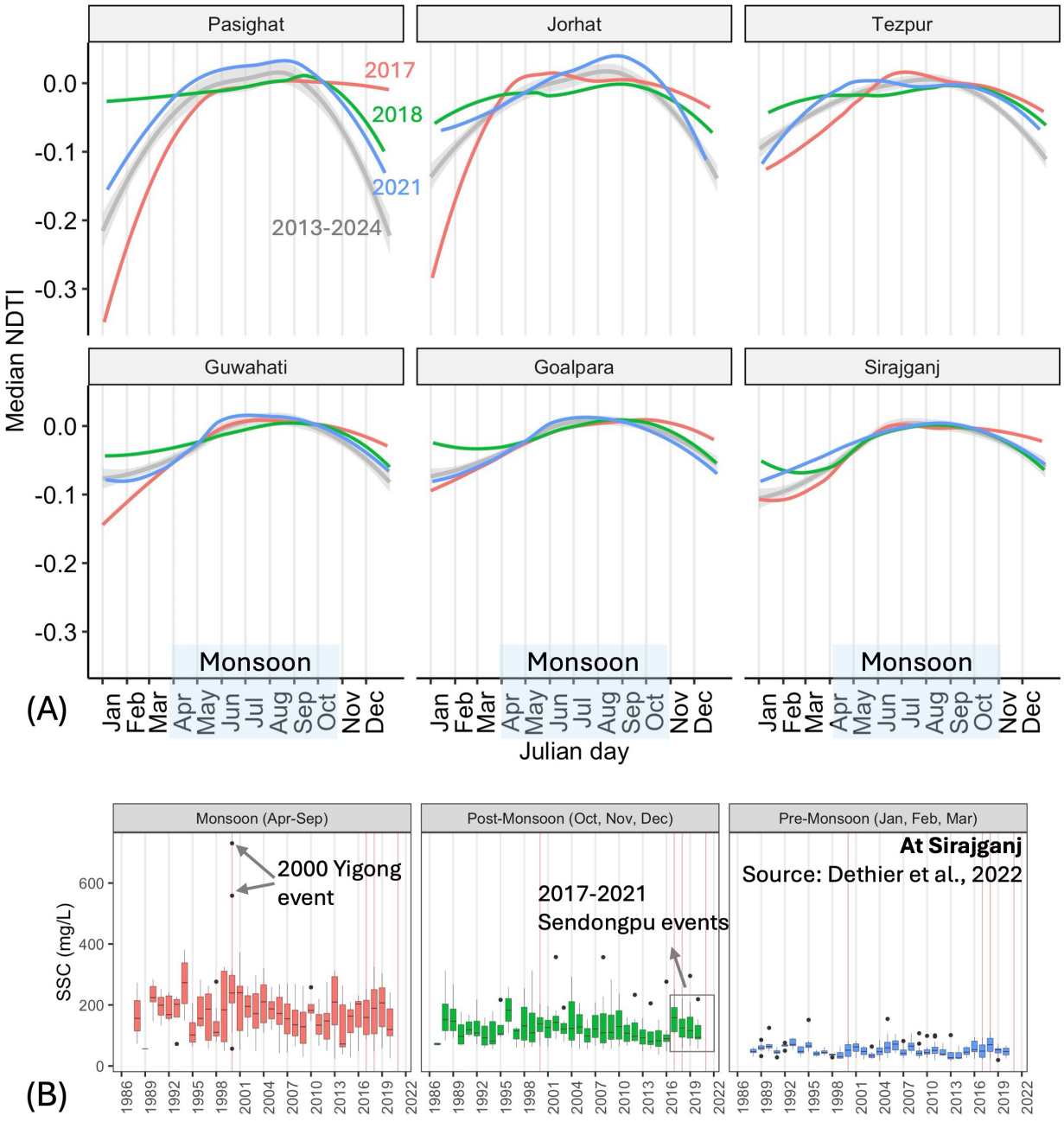


Figure 4: (A) Annual variation of median NDTI, smoothed using the Locally Estimated Scatterplot Smoothing (LOESS) method. Following October 2017, median NDTI exhibited deviations from the 2013–2024 average. This deviation gradually diminished in downstream nodes. Refer to SI Figure S3 for the entire raw time series. (B) Boxplot of suspended sediment concentration at Sirajganj in the delta, separated by seasons (Date source: Dethier et al. (2022)). Boxes represent the interquartile range, while black dots indicate outliers. Red vertical lines indicate years of mass-wasting events.

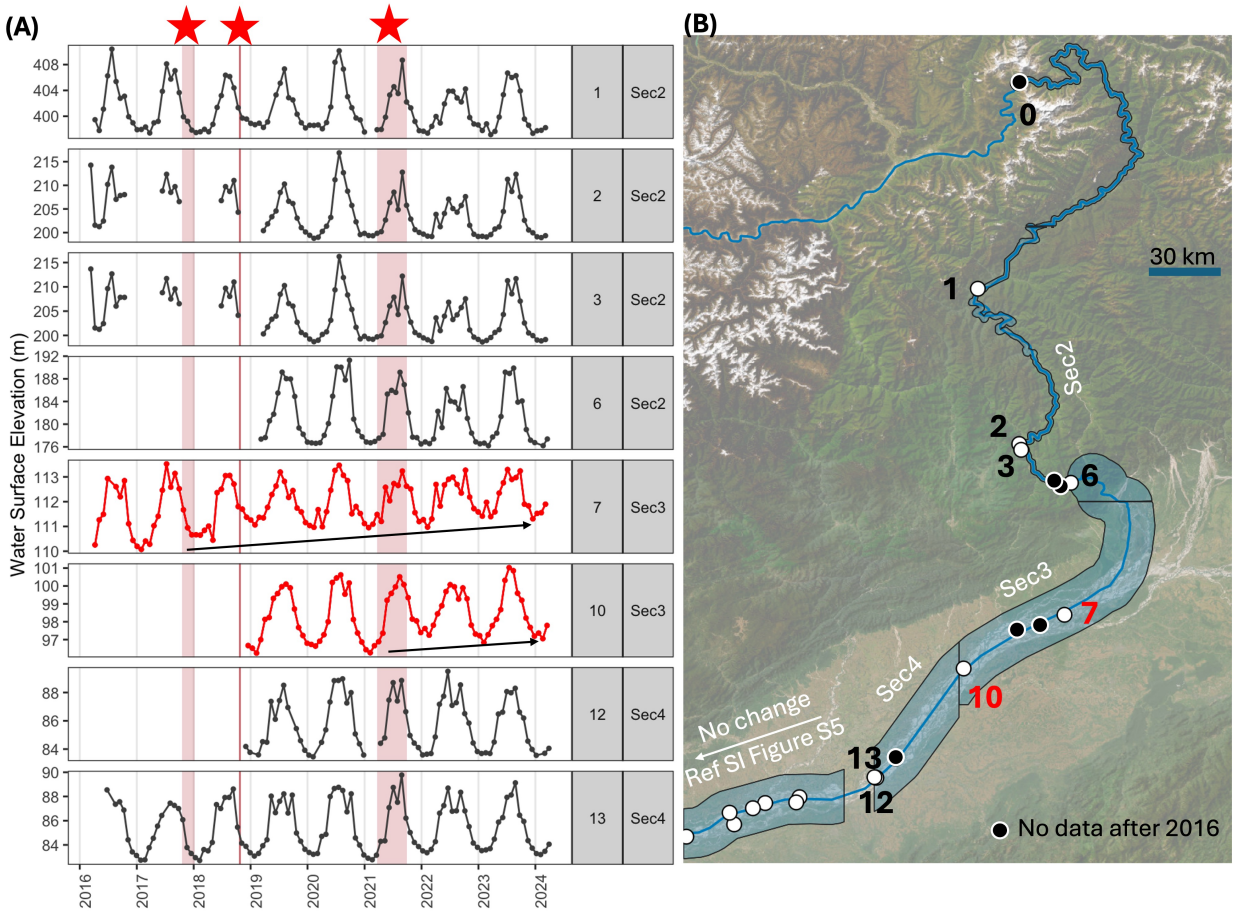


Figure 5: (A) Water surface elevation for selected locations in Sec2, Sec3 and Sec4. Red stars indicate the occurrence of mass-wasting events in the Sendongpu. Lineplots in (A) correspond to locations shown in (B). Only locations, annotated with numbers, have data after 2016, and are presented in lineplot. Refer to SI Figure S5 for entire time series for all locations. Basemap source: Esri, Maxar, Earthstar Geographics, and the GIS User Community.

### 4.3 % Sandbar area

Figure 6 shows the % Sandbar area variation in Sec1, Sec2 and Sec3. SI Figure S6 shows the time series of all other locations. Consistent with the water surface elevation data, the % Sandbar area shows an increasing trend in Sec3. Following the 2017 event, the percentage of sandbar area increased steadily from 20% to 35% during the non-monsoon months from 2018 to 2020 (Figure 6). However, after 2020, the events of 2021 did not result in a further increase in sandbar area. Instead, the exposed sandbar area decreased from 35% to 25%, followed by a subsequent increase to approximately 30%.

### 4.4 SAR maximum water extent

As there were observed changes in the Sec3, we investigated the water extent in that section (Figure 7). The black pixels in the SAR imagery indicate low backscatter, which is characteristic of water due to its smooth surface (specular reflection) and high dielectric constant. Notably, the water extent increased sharply downstream of Pasighat in 2017 (Figure 7), likely triggered by the 2017 Sendongpu mass-wasting event. This trend persisted in subsequent years, with channel width continuing to increase due to ongoing bank and bar erosion. For instance, the eastern channel width expanded from approximately 2.5 km in 2015 to 5 km by 2024. Similarly, the area of an in-channel sandbar decreased significantly, shrinking from 90 $km^2$ to 37 $km^2$.

## 5 Discussion

### 5.1 Spatial and temporal extent of river response to mass wasting

Mass wasting events generate large quantities of sediment that rivers must either accommodate or transport. Increasing trends of turbidity, water surface elevation and sandbar area are observed in approximately 100 km reach of Sec3 (Figure 8D). Sec3 is located just downstream of the mountain front where the Siang River emerges and transitions into the braided belt of the Brahmaputra (Figures 8A and 3C). Further downstream, in sections like Sec7 (Figure 8C), an increase in turbidity was not coincident with the changes in planform or water surface elevation. Near the delta in Sec10 (Figure 8B), suspended sediment concentrations during post-monsoon months were higher compared to the year preceding the mass-wasting event. These observations suggest that planform changes are primarily limited to the upstream sections near the mountain front, but suspended sediment

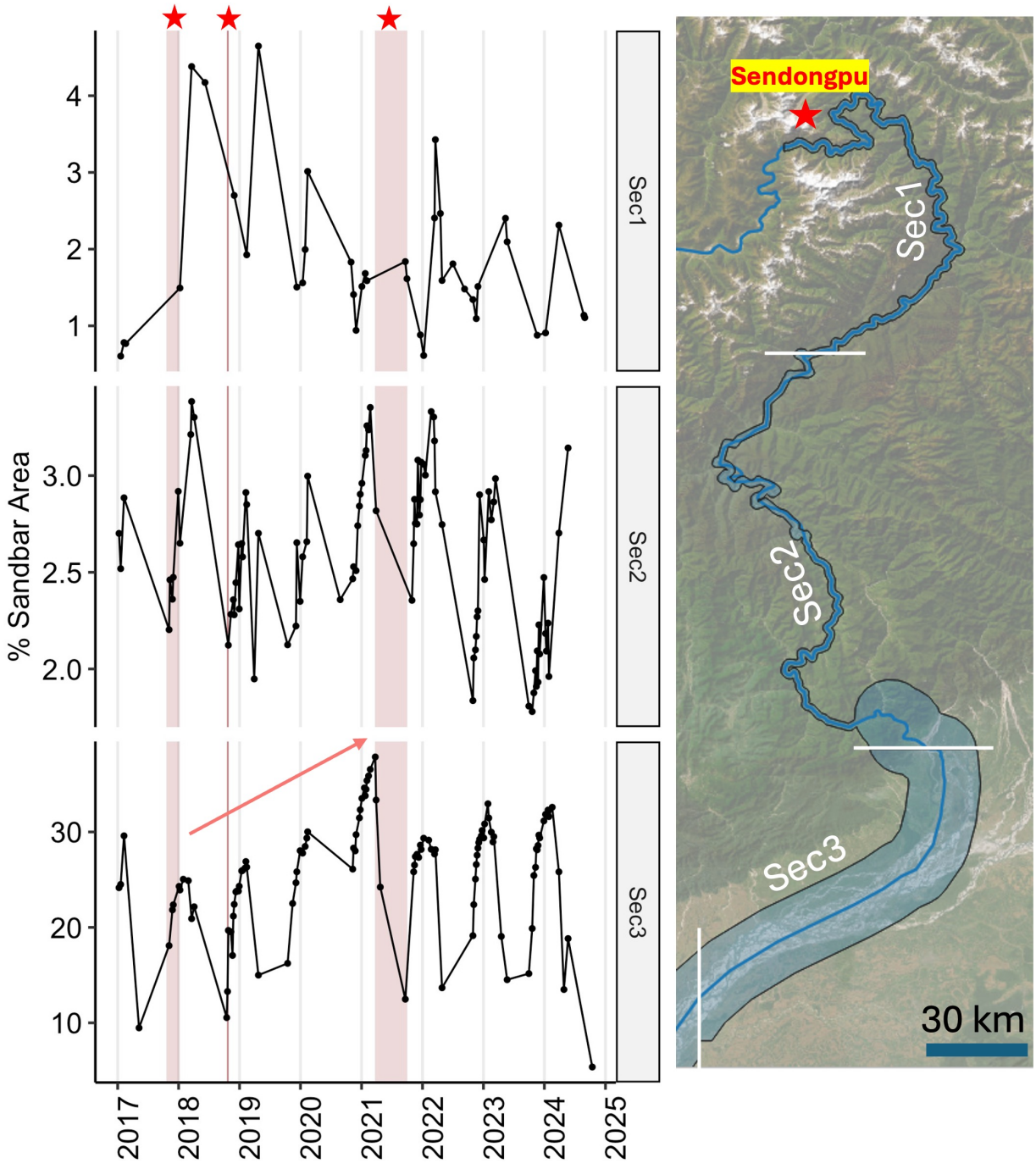


Figure 6: Percentage of sandbar area in Sec1, Sec2 and Sec3. Vertical red area and red star indicate the timing of the mass-wasting events. Basemap source: Esri, Maxar, Earthstar Geographics, and the GIS User Community.

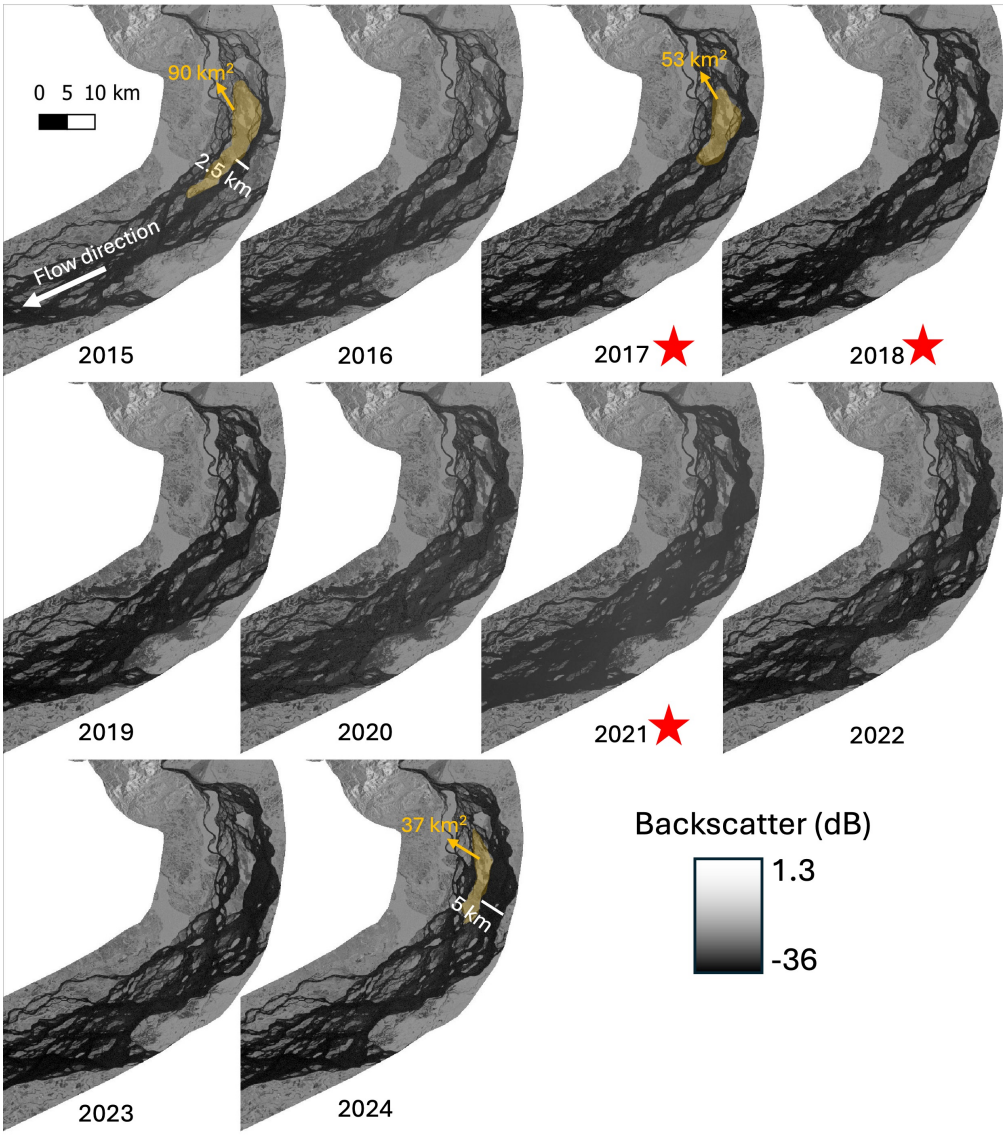


Figure 7: Maximum water extent derived from SAR imagery for each year in the Sec3 region downstream of Pasighat.

can be traced far downstream, reaching approximately 1300 km to the delta (Figure 8B). Although attributing downstream signals to specific mass-wasting events in such a large and dynamic fluvial system is inherently challenging, the temporal coincidence between the mass-wasting period and the observed increase in turbidity suggests a strong link. Sediment storage and delayed remobilization within the river network may also modulate the downstream signal (e.g., **?**), particularly when multiple disturbances occur within a short time span.

This reason of far-scale transport of the suspended sediments can be linked to the grain size. Suspended sediments in the Brahmaputra River typically range from 10–30 $\mu$m (SI Figure S7, Dixit et al., 2023) and are ubiquitous in the water column, regardless of seasonal discharge variations (Garzanti et al., 2011; Lupker et al., 2011). These fine particles may be classified as wash load, which, by definition, can be transported over long distances downstream and can retain signatures of mass-wasting deposits. For instance, based on the sediment provenance analysis, Dixit et al. (2023) suspected the 2021 Sendongpu event's sedimentary signature in suspended sediments sampled at Guwahati.

In contrast, the coarse sediments found on Brahmaputra's sandbars typically range from 100–300 $\mu$m (SI Figure S7, Garzanti et al., 2011; Dixit et al., 2024). These coarser grains are transported as uniform or graded suspension near the riverbed, primarily during monsoon periods (Dixit et al., 2024). Due to their higher grain size and limited transport efficiency, coarse sediments are predominantly deposited near the mountain front or tributary confluences, where they induce morphological disturbances such as channel widening and bar configuration, as observed in Sec3.

Nonetheless, the far-scale transport of suspended sediment to the delta is remarkable. Such a phenomenon aligns with efficient sediment evacuation in the Brahmaputra basin reported previously (Singh and France-Lanord, 2002; Garzanti et al., 2004; Finnegan et al., 2008). Notably, the area between Sendongpu and Sec3 brackets the Eastern Syntaxis zone of the Himalayas (Figure 8A). This region is characterized by a steep elevation drop from approximately 3000 m to 150 m over a longitudinal distance of 400 km. Such a sharp topographic gradient promotes the efficient transport of sediments through the Himalayan valley (Sec1 and Sec2). These sediments are then deposited at the beginning of the braided belt in Sec3 within a stretch of approximately 100 km, where the river's energy dissipates abruptly due to the sudden change in slope. Provenance analyses of the Brahmaputra sands identify Sec3 as a tectonic trap that stores substantial volumes of upstream sediment (Yu et al., 2025).

In summary, while fine sediments from a mass-wasting event 1300 km upstream can travel to

the delta and elevate turbidity along the entire course (Figure 9), coarse sediments are primarily responsible for morphological disturbances within the first approximately 100 km downstream of the mountain front. Consequently, mass-wasting events not only increase turbidity but also raise water surface elevation and expand sandbar area in this critical reach.

## 5.2 Implications of mass-wasting for flood risk

Our analysis reveals a significant increase in flood extent downstream of the mountain front (Sec3) following the 2017 event (Figure 7 and SI Figure S8A). Optical imagery from non-monsoon months further highlights an increase in braided-channel width and exposed sandbar area, both triggered by the 2017 Sendongpu mass-wasting events (SI Figure S8B). This increase in water extent cannot be attributed to hydrological factors such as rainfall, as the rainfall distribution over this period shows no notable variability (SI Figure S9). Instead, the observed changes in maximum water extent are clearly linked to the mass-wasting events.

Mass-wasting events led to two main types of sediment deposition: vertical channel infilling and lateral sedimentation along bars and banks. Channel infilling likely raised the water surface and increased water extent, while lateral deposition may have contributed to overbank buildup and the formation of alluvial ridges, which can limit flood spread. At the same time, enhanced lateral mobility through bank and bar erosion may also have expanded the water extent. Although the relative influence of these processes is difficult to quantify with the available data, the 2017 mass-wasting event appears to be the key trigger. This event deposited a large volume of sediment in Sec3, as indicated by the increase in sandbar area and water surface elevation. These changes may have altered the sedimentary–hydromorphic regime of Sec3, promoting additional bank and bar erosion, and collectively contributing to the observed increase in maximum water extent. However, by 2021, the sandbar area declined, likely due to the reworking of bars as channels widened and became more interconnected (SI Figure S8B, 2021–2022). This adjustment phase reflects the transition from initial sediment deposition to a more dynamic, laterally mobile system.

Interestingly, the eastern channel of the river exhibited more pronounced widening compared to the western channel. Such variability near the mountain front is well-documented in Himalayan rivers (e.g., Sinha, 2009), and often depends on factors such as longitudinal versus across-channel slope and the relative elevation of both channels (Gearon et al., 2024). Although high-resolution elevation data are unavailable to confirm these factors definitively, our observations align with long-term trends. For example, Devi et al. (2016) documented an increase in maximum channel width

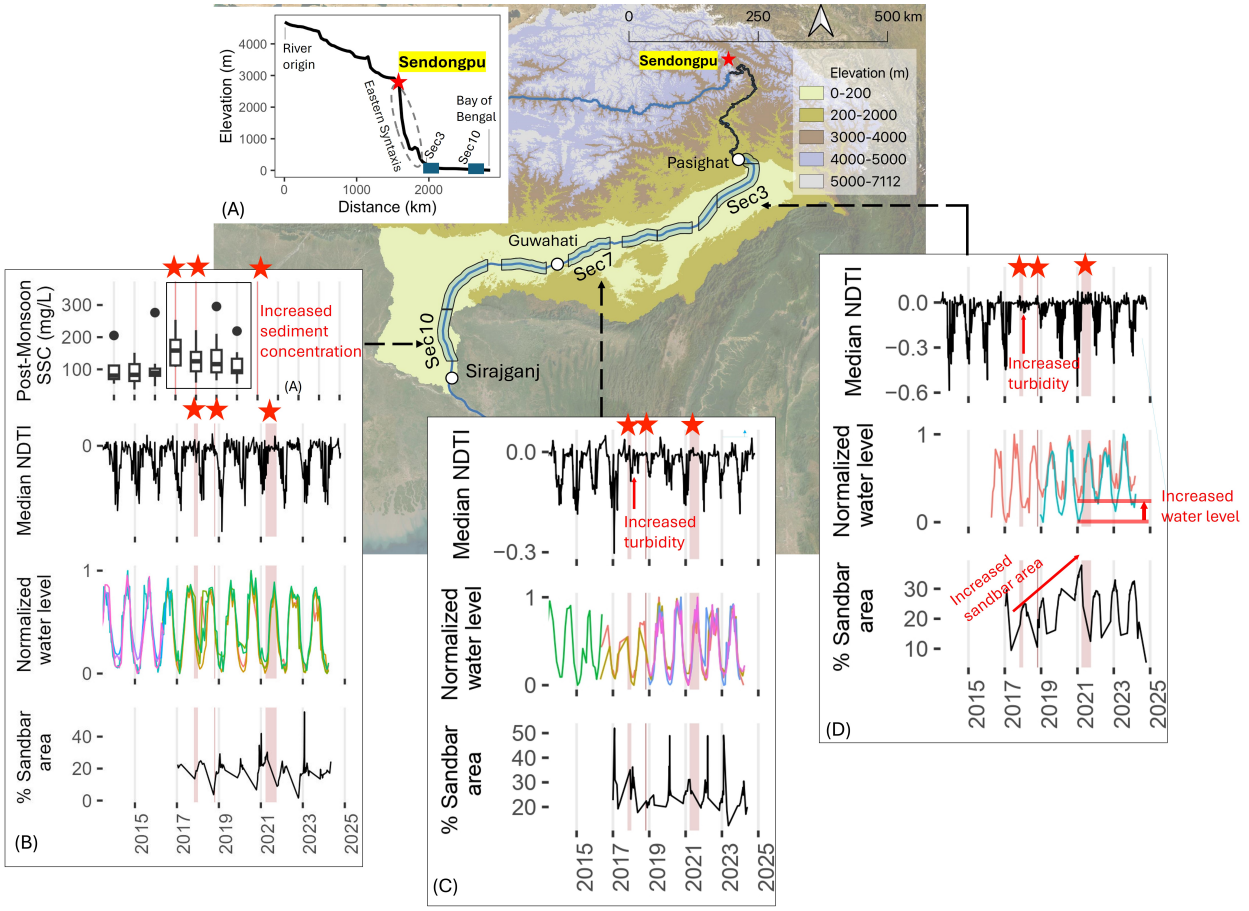


Figure 8: Map depicting elevation values across the Brahmaputra basin. (A) Longitudinal profile of the Yarlung-Siang-Brahmaputra River, with key locations highlighted along the profile. The region between Sendongpu and Pasighat marks the Eastern Syntaxis, characterized by a sharp elevation gradient. (B), (C), and (D) illustrate the variation in key parameters—such as turbidity, suspended sediment concentration and water surface elevation—in response to mass-wasting events at Sec10, Sec7 and Sec3, respectively. Different colors in the normalized water level plot indicate different locations in their respective sections. Basemap source: Esri, Maxar, Earthstar Geographics, and the GIS User Community.

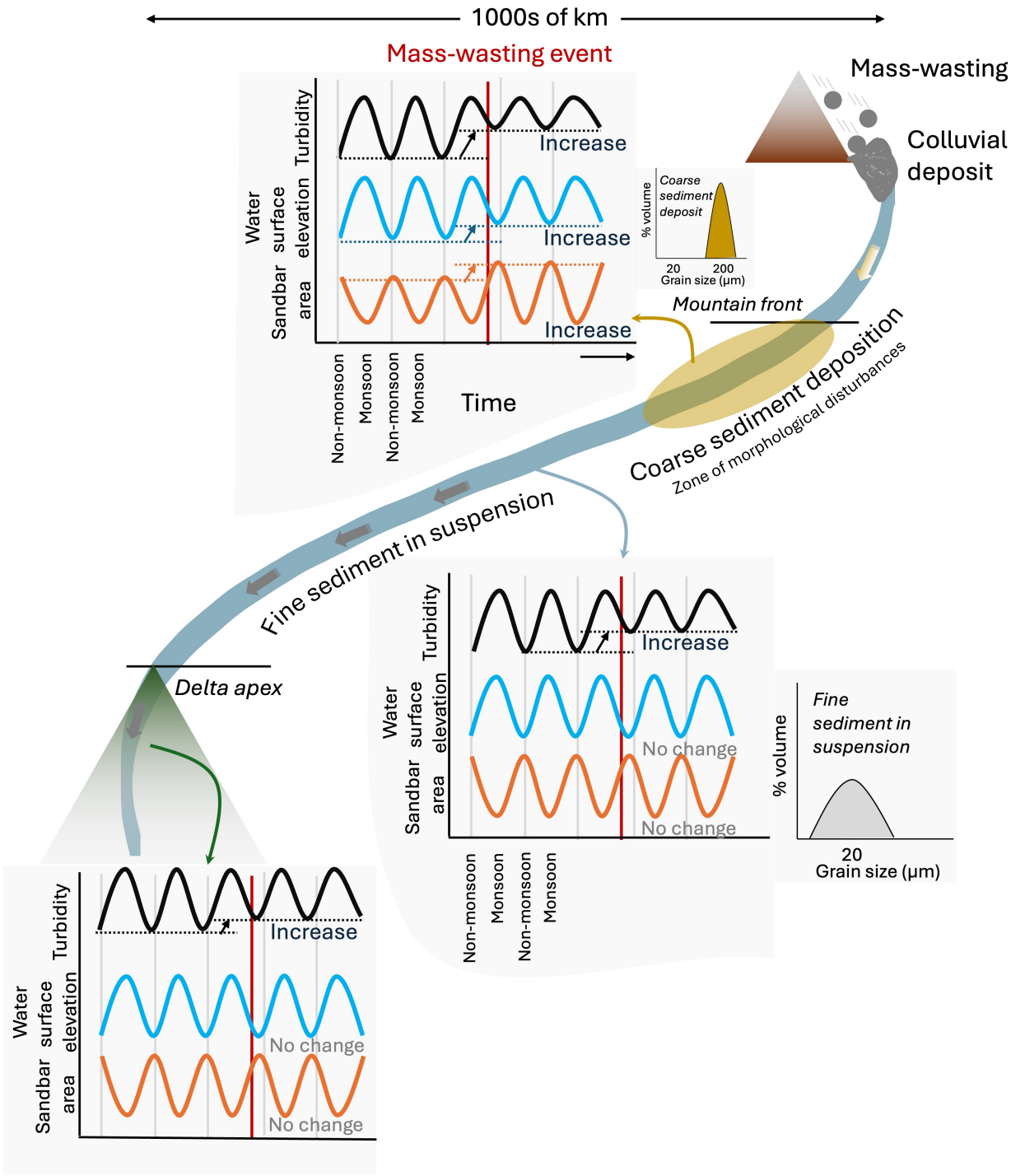


Figure 9: Conceptual figure illustrating the key findings. Near the mountain front, coarse sediments from mass-wasting events generate morphological disturbances, raising water surface elevations and increasing sandbar area. In contrast, fine sediments are transported across the basin and reach the delta, even in a large river system such as the Brahmaputra.

Table 2: Comparison of Sendongpu (2018) and Yigong (2000) mass-wasting related events. Data source. Data sources are Guo et al. (2023); Li et al. (2024); Chen et al. (2020).

| | **Sendongpu event 2018** | **Yigong event 2000** |
|---|---|---|
| Lake volume | $490 \times 10^6$ $m^3$ | $3000 \times 10^6$ $m^3$ |
| Colluvial deposit volume | $35 \times 10^6$ $m^3$ | $300 \times 10^6$ $m^3$ |
| Breakage | Partial breakage, river maintained flow | Sudden breakage, outburst flood |
| Response | Increased turbidity in subsequent post-monsoon | High turbidity during monsoon of 2000 |

from 1 km to 2.7 km between 1966–1972 and 2012 in the Sec3. Yu et al. (2025) report the Sec3 region as the tectonic trap which stores upstream sediments. Therefore, such morphological changes are more likely to occur.

### 5.3 Comparison of Yigong and Sendongpu events

The differing impacts of the Yigong and Sendongpu events on river morphology and sediment dynamics are notable and can provide key understanding of how rivers respond to large-scale mass-wasting events. The characteristics of these events and responses are summarized in Table 2. The Yigong event of 2000 was a significantly larger outburst event, characterized by the breaching of a $3000 \times 10^6$ $m^3$ lake and a $300 \times 10^6$ $m^3$ landslide dam. In contrast, the Sendongpu events, such as the 2018 outburst, involved a $490 \times 10^6$ $m^3$ lake and a much smaller debris dam of approximately $35 \times 10^6$ $m^3$ (Chen et al., 2020; Li et al., 2024). The subsequent outburst of the Yigong event caused a sudden influx of sediments, leading to sediment concentrations three times higher than usual downstream, reaching as far as approximately 1300 km to the delta (Figure 4B). In contrast, the rates of sediment mobilization from Sendongpu events were relatively slower and lacked a sudden outburst, resulting in a more subdued and gradual sediment response.

## 6 Conclusion

Investigation of river response to mass-wasting events is often limited at reach- or catchment-scale. In this study, we investigated the river response of a large river to major mass-wasting events in the Eastern Himalaya over extended spatial (approximately 1000 of kilometer) and temporal (years) scales, leveraging an advanced cloud computing platform, Google Earth Engine. We examined how these events leave signatures in suspended sediment dynamics, water surface elevation, river sand-

bar morphology and flood inundation.

The Eastern Syntaxis in the Himalaya is a region of unique and large-scale mass-wasting processes both in modern and ancient time scales. Over the past seven years, the Sendongpu glacier alone has eroded approximately 50, 180 and 329 × $10^6$ $m^3$ of sediment during three major events in 2017, 2018 and 2021, respectively. Additionally, the nearby Yigong event eroded 300 × $10^6$ $m^3$ in 2000 following a landslide outburst flood.

Our findings demonstrate that suspended sediment signatures from mass-wasting events can be traced up to approximately 1000 km downstream, reaching the delta. However, coarse sediments primarily influence river planform changes in the approximately 100 km reach near the mountain front, where the river starts to establish a braided belt. In this region, we observed an increase in sandbar area of between 20% and 35% following the 2017 events. This morphological change coincided with elevated water surface elevation and high flood inundation, suggesting significant channel infilling.

Comparing the Sendongpu and Yigong events highlights how the character of an individual event can define the river's response. For example, the 2000 Yigong event, a single large and sudden outburst, led to a far-reaching but short-lived sediment response. In contrast, the Sendongpu events, which were smaller, slower and more frequent, produced a prolonged but less intense river response, with sediment retained in valleys and gradually mobilized over time.

While we quantified the spatial extent of river responses to mass-wasting events, future studies should focus on quantifying sediment budgets specific to these events. This includes determining the volume of sediment generated by mass wasting and assessing its partitioning among storage in valleys, floodplains and river channels. Such data are critical for understanding the impacts of mass-wasting events on flood management or hydropower planning in regions that are already flood-prone and earmarked for extensive hydropower development. These changes are likely to reshape river systems in ways that we have not yet been able to fully observe or predict.

# References

Ahrendt, S., Horner-Devine, A. R., Collins, B. D., Morgan, J. A., and Istanbulluoglu, E. (2022). Channel Conveyance Variability can Influence Flood Risk as Much as Streamflow Variability in Western Washington State. *Water Resources Research*, 58(6):e2021WR031890.

Ashworth, P. J. and Lewin, J. (2012). How do big rivers come to be different? *Earth-Science Reviews*, 114(1):84–107.

Bailey, L. P., Shugar, D. H., Tilston, M., Hubbard, S. M., Giesbrecht, I., Del Bel Belluz, J., Jackson, J. M., Clare, M. A., Cartigny, M. J. B., Açıkalın, S., Hage, S., Talling, P. J., Basiuk, H., Menounos, B., and Geertsema, M. (2025). Land-To-Sea Sediment Fluxes From a Major Glacial Lake Outburst Flood Were Stepped Rather Than Instantaneous. *Journal of Geophysical Research: Earth Surface*, 130(4):e2024JF008126.

Bennett, G. L., Panici, D., Rengers, F. K., Kean, J. W., and Rathburn, S. L. (2025). Landslide-channel feedbacks amplify channel widening during floods. *npj Natural Hazards*, 2(1):7.

Brown, C. F., Brumby, S. P., Guzder-Williams, B., Birch, T., Hyde, S. B., Mazzariello, J., Czerwinski, W., Pasquarella, V. J., Haertel, R., Ilyushchenko, S., et al. (2022). Dynamic world, near real-time global 10 m land use land cover mapping. *Scientific Data*, 9(1):251.

Campbell, J. B. and Wynne, R. H. (2011). *Introduction to remote sensing*. Guilford Press.

Carrivick, J. L. and Tweed, F. S. (2016). A global assessment of the societal impacts of glacier outburst floods. *Global and Planetary Change*, 144:1–16.

Chen, C., Zhang, L., Xiao, T., and He, J. (2020). Barrier lake bursting and flood routing in the Yarlung Tsangpo Grand Canyon in October 2018. *Journal of Hydrology*, 583:124603.

Croissant, T., Lague, D., Steer, P., and Davy, P. (2017). Rapid post-seismic landslide evacuation boosted by dynamic river width. *Nature Geoscience*, 10(9):680–684.

Dai, L., Scaringi, G., Fan, X., Yunus, A. P., Liu-Zeng, J., Xu, Q., and Huang, R. (2021). Coseismic Debris Remains in the Orogen Despite a Decade of Enhanced Landsliding. *Geophysical Research Letters*, 48(19):e2021GL095850.

DeLisle, C., Yanites, B. J., Chen, C.-Y., Shyu, J. B. H., and Rittenour, T. M. (2022). Extreme event-driven sediment aggradation and erosional buffering along a tectonic gradient in southern Taiwan. *Geology*, 50(1):16–20.

Dethier, E. N., Renshaw, C. E., and Magilligan, F. J. (2022). Rapid changes to global river suspended sediment flux by humans. *Science*, 376(6600):1447–1452.

Devi, R. K. M., Bhakuni, S. S., Phukan, M. K., and Duarah, R. (2016). Tectonic forcing of drainages and geomorphic features developed across himalayan mountain frontal part of western limb of siang antiform, arunachal himalaya. *Environmental Earth Sciences*, 75(5):413.

Dixit, A., Dutta, S., and Mahanta, C. (2024). Grain-size gap and downstream fining revealed in less chemically altered Brahmaputra Sandbars. *Journal of Soils and Sediments*, 24:1002–1018.

Dixit, A., von Eynatten, H., Schönig, J., Karius, V., Mahanta, C., and Dutta, S. (2023). Intra-seasonal variability in sediment provenance and transport processes in the brahmaputra basin. *Journal of Geophysical Research: Earth Surface*, 128(6):e2023JF007105.

Dong, X., Wang, X., Yang, L., Zhao, Z., Van Balen, R., Miao, X., Liu, T., Vandenberghe, J., Pan, B., Gibling, M., and Lu, H. (2024). Quantitative assessment of the erosion and deposition effects of landslide-dam outburst flood, eastern himalaya. *Scientific Reports*, 14(1):7038.

Dubey, A. K. and Singh, R. (2021). Flood assessment in the brahmaputra river using microwave remote sensing and hydrological modelling. *Journal of Geomatics*, 15(2):263–267.

Dunn, O. J. (1964). Multiple comparisons using rank sums. *Technometrics*, 6(3):241–252.

Fidan, S., Tanyaş, H., Akbaş, A., Lombardo, L., Petley, D. N., and Görüm, T. (2024). Understanding fatal landslides at global scales: A summary of topographic, climatic, and anthropogenic perspectives. *Natural Hazards*, 120(7):6437–6455.

Finnegan, N. J., Hallet, B., Montgomery, D. R., Zeitler, P. K., Stone, J. O., Anders, A. M., and Yuping, L. (2008). Coupling of rock uplift and river incision in the Namche Barwa-Gyala Peri massif, Tibet. *Bulletin of the Geological Society of America*, 120(1-2):142–155.

Fordham, E. M., Pfeiffer, A. M., Bunn, A. G., and Novak, S. J. (2023). Recurrent debris flows and their downstream fate: Geomorphic drivers of an anomalous sediment load, Suiattle River, Washington State, USA. *Earth Surface Processes and Landforms*, 48(7):1307–1320.

Froude, M. J. and Petley, D. N. (2018). Global fatal landslide occurrence from 2004 to 2016. *Natural Hazards and Earth System Sciences*, 18(8):2161–2181.

Funk, C., Peterson, P., Landsfeld, M., Pedreros, D., Verdin, J., Shukla, S., Husak, G., Rowland, J., Harrison, L., Hoell, A., et al. (2015). The climate hazards infrared precipitation with stations—a new environmental record for monitoring extremes. *Scientific data*, 2(1):1–21.

Galy, A. and France-Lanord, C. (2001). Higher erosion rates in the Himalaya: Geochemical constraints on riverine fluxes. *Geology*, 29(1):23–26.

Garzanti, E., Andó, S., France-Lanord, C., Censi, P., Vignola, P., Galy, V., and Lupker, M. (2011). Mineralogical and chemical variability of fluvial sediments 2. suspended-load silt (ganga–brahmaputra, bangladesh). *Earth and Planetary Science Letters*, 302(1-2):107–120.

Garzanti, E., Vezzoli, G., Andò, S., France-Lanord, C., Singh, S. K., and Foster, G. (2004). Sand petrology and focused erosion in collision orogens: The Brahmaputra case. *Earth and Planetary Science Letters*, 220(1-2):157–174.

Gayer, E., Lucas, A., Michon, L., and Gougeon, M. (2025). Evidence for Erosional Efficiency of Extreme Precipitation Events at a Multi- Decadal Time Scale. *Journal of Geophysical Research: Earth Surface*, 130(3):e2024JF007818.

Gearon, J. H., Martin, H. K., DeLisle, C., Barefoot, E. A., Mohrig, D., Paola, C., and Edmonds, D. A. (2024). Rules of river avulsion change downstream. *Nature*, 634(8032):91–95.

Goswami, D. C. (1985). Brahmaputra river, assam, india: Physiography, basin denudation, and channel aggradation. *Water Resources Research*, 21(7):959–978.

Graf, E. L. S., Sinclair, H. D., Attal, M., Gailleton, B., Adhikari, B. R., and Baral, B. R. (2024). Geomorphological and hydrological controls on sediment export in earthquake-affected catchments in the nepal himalaya. *Earth Surface Dynamics*, 12(1):135–161.

Guo, C., Yuan, H., Wu, R., Yan, Y., and Yang, Z. (2023). Research review and prospects of the 2000 giant Yigong long-runout landslide: Volume, formation mechanism and recurrence period, Tibetan plateau, China. *Frontiers in Earth Science*, 10:1017611.

Hovius, N., Meunier, P., Lin, C.-W., Chen, H., Chen, Y.-G., Dadson, S., Horng, M.-J., and Lines, M. (2011). Prolonged seismically induced erosion and the mass balance of a large earthquake. *Earth and Planetary Science Letters*, 304(3-4):347–355.

Hu, K., Zhang, X., Tang, J., and Liu, W. (2018). Potential danger of dammed lakes induced by the 2017 Ms6. 9 Mifflin earthquake in the Tsangpo gorge. In *5th International Conference Debris Flows: Disasters, Risk, Forecast, Protection*, pages 97–104. Publishing House “Universal” Tbilisi.

Hu, K., Zhang, X., You, Y., Hu, X., Liu, W., and Li, Y. (2019). Landslides and dammed lakes triggered by the 2017 ms6.9 milin earthquake in the tsangpo gorge. *Landslides*, 16(5):993–1001.

Islam, M. R., Begum, S. F., Yamaguchi, Y., and Ogawa, K. (1999). The Ganges and Brahmaputra rivers in Bangladesh: basin denudation and sedimentation. *Hydrological Processes*, 13(17):2907–2923.

Jain, V., Dixit, A., Singh, A., and Tandon, S. K. (2025). Unravelling sediment sources and sinks in the large Ganga River system. *Environmental Research Letters*, 20(7):074073.

Jones, J. N., Boulton, S. J., Stokes, M., Bennett, G. L., and Whitworth, M. R. Z. (2021). 30-year record of Himalaya mass-wasting reveals landscape perturbations by extreme events. *Nature Communications*, 12(1):6701.

Kääb, A. and Girod, L. (2023). Brief communication: Rapid $\sim 335 \times 10^6\,\mathrm{m}^3$ bed erosion after detachment of the sedongpu glacier (tibet). *The Cryosphere*, 17(6):2533–2541.

Kääb, A., Jacquemart, M., Gilbert, A., Leinss, S., Girod, L., Huggel, C., Falaschi, D., Ugalde, F., Petrakov, D., Chernomorets, S., et al. (2021). Sudden large-volume detachments of low-angle mountain glaciers–more frequent than thought? *The Cryosphere*, 15(4):1751–1785.

Kashyap, A., Cook, K. L., and Behera, M. D. (2025). Geomorphic imprint of high-mountain floods: Insights from the 2022 hydrological extreme across the upper Indus River catchment in the northwestern Himalayas. *Earth Surface Dynamics*, 13(1):147–166.

Keefer, D. K. (1999). Earthquake-induced landslides and their effects on alluvial fans. *Journal of Sedimentary Research*, 69(1):84–104.

Korup, O. (2004). Landslide-induced river channel avulsions in mountain catchments of southwest New Zealand. *Geomorphology*, 63(1):57–80.

Kruskal, W. H. and Wallis, W. A. (1952). Use of ranks in one-criterion variance analysis. *Journal of the American statistical Association*, 47(260):583–621.

Lacaux, J., Tourre, Y., Vignolles, C., Ndione, J., and Lafaye, M. (2007). Classification of ponds from high-spatial resolution remote sensing: Application to rift valley fever epidemics in senegal. *Remote sensing of environment*, 106(1):66–74.

Lang, K. A., Huntington, K. W., and Montgomery, D. R. (2013). Erosion of the tsangpo gorge by megafloods, eastern himalaya. *Geology*, 41(9):1003–1006.

Li, D., Lu, X., Walling, D. E., Zhang, T., Steiner, J. F., Wasson, R. J., Harrison, S., Nepal, S., Nie, Y., Immerzeel, W. W., Shugar, D. H., Koppes, M., Lane, S., Zeng, Z., Sun, X., Yegorov, A., and Bolch, T. (2022). High mountain asia hydropower systems threatened by climate-driven landscape instability. 15(7):520–530.

Li, G. K., West, A. J., Jin, Z., Qiu, H., Zhang, F., Wang, J., Hammond, D. E., Densmore, A. L., Hilton, R. G., Dong, S., Atwood, A., Fischer, W. W., and Lamb, M. P. (2025). Large riverbed sediment flux sustained for a decade after an earthquake. *Nature*, 644(8076):398–403.

Li, W., Zhao, B., Lu, H., Li, Z., Yu, W., Zhou, S., and Xu, Q. (2024). More mass wasting activities reported in Sedongpu gully of Tibetan Plateau, China. *Journal of Rock Mechanics and Geotechnical Engineering*.

Li, Y., Wright, D. B., and Byrne, P. K. (2020). The Influence of Tropical Cyclones on the Evolution of River Conveyance Capacity in Puerto Rico. *Water Resources Research*, 56(9):e2020WR027971.

Lupker, M., France-Lanord, C., Lavé, J., Bouchez, J., Galy, V., Métivier, F., Gaillardet, J., Lartiges, B., and Mugnier, J.-L. (2011). A rouse-based method to integrate the chemical composition of river sediments: Application to the ganga basin. *Journal of Geophysical Research*, 116(F4).

Lupker, M., Lavé, J., France-Lanord, C., Christl, M., Bourlès, D., Carcaillet, J., Maden, C., Wieler, R., Rahman, M., Bezbaruah, D., and Xiaohan, L. (2017). 10 be systematics in the tsangpo-brahmaputra catchment: the cosmogenic nuclide legacy of the eastern himalayan syntaxis. *Earth Surface Dynamics*, 5(3):429–449.

Major, J. J., Mosbrucker, A. R., and Spicer, K. R. (2018). Sediment Erosion and Delivery from Toutle River Basin After the 1980 Eruption of Mount St. Helens: A 30-Year Perspective. In Crisafulli, C. M. and Dale, V. H., editors, *Ecological Responses at Mount St. Helens: Revisited 35 Years after the 1980 Eruption*, pages 19–44. Springer, New York, NY.

Milliman, J. D. and Farnsworth, K. L. (2011). *River Discharge to the Coastal Ocean*. Cambridge University Press, Cambridge.

Nandi, K. K., Pradhan, C., Dutta, S., and Khatua, K. K. (2022). How dynamic is the brahmaputra? understanding the process–form–vegetation interactions for hierarchies of energy dissipation. *Ecohydrology*, 15(3):e2416.

Panda, S., Kumar, A., Das, S., Devrani, R., Rai, S., Prakash, K., and Srivastava, P. (2020). Chronology and sediment provenance of extreme floods of Siang River (Tsangpo-Brahmaputra River valley), northeast Himalaya. *Earth Surface Processes and Landforms*, 45(11):2495–2511.

Pekel, J.-F., Cottam, A., Gorelick, N., and Belward, A. S. (2016). High-resolution mapping of global surface water and its long-term changes. *Nature*, 540(7633):418–422.

Rinaldi, M., Amponsah, W., Benvenuti, M., Borga, M., Comiti, F., Lucía, A., Marchi, L., Nardi, L., Righini, M., and Surian, N. (2016). An integrated approach for investigating geomorphic response to extreme events: Methodological framework and application to the October 2011 flood in the Magra River catchment, Italy. *Earth Surface Processes and Landforms*, 41(6):835–846.

SANDRP (2017). Muddy Siang is sign of danger ahead, wake up call for Indian authorities.

Sarma, J. N. and Acharjee, S. (2018). A study on variation in channel width and braiding intensity of the brahmaputra river in assam, india. *Geosciences*, 8(9):343.

Sattar, A., Cook, K. L., Rai, S. K., Berthier, E., Allen, S., Rinzin, S., Van Wyk de Vries, M., Haeberli, W., Kushwaha, P., Shugar, D. H., Emmer, A., Haritashya, U. K., Frey, H., Rao, P., Gurudin, K. S. K., Rai, P., Rajak, R., Hossain, F., Huggel, C., Mergili, M., Azam, M. F., Gascoin, S., Carrivick, J. L., Bell, L. E., Ranjan, R. K., Rashid, I., Kulkarni, Anil. V., Petley, D., Schwanghart, W., Watson, C. S., Islam, N., Gupta, M. D., Lane, S. N., and Bhat, S. Y. (2025). The Sikkim flood of October 2023: Drivers, causes and impacts of a multihazard cascade. *Science*, 0(0):eads2659.

Schwatke, C., Dettmering, D., Bosch, W., and Seitz, F. (2015). Dahiti–an innovative approach for estimating water level time series over inland waters using multi-mission satellite altimetry. *Hydrology and Earth System Sciences*, 19(10):4345–4364.

Sharma, S., Talchabhadel, R., Nepal, S., Ghimire, G. R., Rakhal, B., Panthi, J., Adhikari, B. R., Pradhanang, S. M., Maskey, S., and Kumar, S. (2023). Increasing risk of cascading hazards in the central Himalayas. *Natural Hazards*, 119(2):1117–1126.

Shugar, D. H., Jacquemart, M., Shean, D., Bhushan, S., Upadhyay, K., Sattar, A., Schwanghart, W., McBride, S., De Vries, M. V. W., Mergili, M., et al. (2021). A massive rock and ice avalanche caused the 2021 disaster at chamoli, indian himalaya. *Science*, 373(6552):300–306.

Singh, S. K. and France-Lanord, C. (2002). Tracing the distribution of erosion in the Brahmaputra watershed from isotopic compositions of stream sediments. *Earth and Planetary Science Letters*, 202(3-4):645–662.

Sinha, R. (2009). The great avulsion of kosi on 18 august 2008. *Current Science*, pages 429–433.

Smith, L. C., Isacks, B. L., Bloom, A. L., and Murray, A. B. (1996). Estimation of discharge from three braided rivers using synthetic aperture radar satellite imagery: Potential application to ungaged basins. *Water Resources Research*, 32(7):2021–2034.

Sofia, G. and Nikolopoulos, E. I. (2020). Floods and rivers: A circular causality perspective. *Scientific Reports*, 10(1):5175.

Stewart, R. J., Hallet, B., Zeitler, P. K., Malloy, M. A., Allen, C. M., and Trippett, D. (2008). Brahmaputra sediment flux dominated by highly localized rapid erosion from the easternmost Himalaya. *Geology*, 36(9):711–714.

Tandon, S. K. and Sinha, R. (2022). Geology of large river systems. *Large Rivers: Geomorphology and Management*, *Second Edition*, pages 7–41.

Taylor, C., Robinson, T. R., Dunning, S., Rachel Carr, J., and Westoby, M. (2023). Glacial lake outburst floods threaten millions globally. *Nature Communications*, 14(1):487.

Times of India (2017). Dark Waters Of The Siang In Arunachal Pradesh High turbidity turning river Siang black: Lab reports Guwahati News - Times of India.

Turzewski, M. D., Huntington, K. W., Licht, A., and Lang, K. A. (2020). Provenance and erosional impact of quaternary megafloods through the yarlung-tsangpo gorge from zircon u-pb geochronology of flood deposits, eastern himalaya. *Earth and Planetary Science Letters*, 535:116113.

Vázquez-Tarrío, D., Ruiz-Villanueva, V., Garrote, J., Benito, G., Calle, M., Lucía, A., and Díez-Herrero, A. (2024). Effects of sediment transport on flood hazards: Lessons learned and remaining challenges. *Geomorphology*, 446:108976.

Wang, J., Jin, Z., Hilton, R. G., Zhang, F., Densmore, A. L., Li, G., and West, A. J. (2015). Controls on fluvial evacuation of sediment from earthquake-triggered landslides. *Geology*, 43(2):115–118.

Westoby, M. J., Dunning, S. A., Carrivick, J. L., Coulthard, T. J., Sain, K., Kumar, A., Berthier, E., Haritashya, U. K., Shean, D. E., Azam, M. F., Upadhyay, K., Koppes, M., McCourt, H. R., and Shugar,

D. H. (2023). Rapid fluvial remobilization of sediments deposited by the 2021 Chamoli disaster, Indian Himalaya. *Geology*.

Xiong, J., Tang, C., Gong, L., Chen, M., Li, N., Shi, Q., Zhang, X., Chang, M., and Li, M. (2022). How landslide sediments are transferred out of an alpine basin: Evidence from the epicentre of the Wenchuan earthquake. *CATENA*, 208:105781.

Xu, H. (2006). Modification of normalised difference water index (ndwi) to enhance open water features in remotely sensed imagery. *International journal of remote sensing*, 27(14):3025–3033.

Yang, Z., Liu, W., Garcia-Castellanos, D., Ruan, H., Luo, J., Zhou, Y., and Sang, Y. (2022). Geomorphic response of outburst floods: Insight from numerical simulations and observations—-The 2018 Baige outburst flood in the upper Yangtze River. *Science of The Total Environment*, 851:158378.

Yanites, B. J., Clark, M. K., Roering, J. J., West, A. J., Zekkos, D., Baldwin, J. W., Cerovski-Darriau, C., Gallen, S. F., Horton, D. E., Kirby, E., Leshchinsky, B. A., Mason, H. B., Moon, S., Barnhart, K. R., Booth, A., Czuba, J. A., McCoy, S., McGuire, L., Pfeiffer, A., and Pierce, J. (2025). Cascading land surface hazards as a nexus in the Earth system. *Science*, 388(6754):eadp9559.

Yanites, B. J., Tucker, G. E., Mueller, K. J., and Chen, Y.-G. (2010). How rivers react to large earthquakes: Evidence from central Taiwan. *Geology*, 38(7):639–642.

Yu, M., Liu, Z., Zhao, Y., Lin, B., Hossain, H. Z., Taral, S., Chakraborty, T., Colin, C., Han, Z., and Wang, C. (2025). Low sediment transport efficiency from the Tibetan Plateau to the Indian Ocean through the Yarlung Zangbo–Brahmaputra–Ganges system. *GSA Bulletin*.

Yunus, A. P., Ishan, A., Magesh, N. S., Sajinkumar, K. S., Scaringi, G., Siva Subramanian, S., and Oommen, T. (2025). Rapid evacuation of suspended sediment loads during landslides in steep gradient rivers. *Environmental Research Communications*, 7(3):031002.

Zhang, S., Zhang, L., Lacasse, S., and Nadim, F. (2016). Evolution of Mass Movements near Epicentre of Wenchuan Earthquake, the First Eight Years. *Scientific Reports*, 6(1):36154.

Zhang, T., Wang, W., An, B., and Wei, L. (2023). Enhanced glacial lake activity threatens numerous communities and infrastructure in the Third Pole. *Nature Communications*, 14(1):8250.

Zhao, B., Li, W., Wang, Y., Lu, J., and Li, X. (2019). Landslides triggered by the Ms 6.9 Nyingchi

earthquake, China (18 November 2017): analysis of the spatial distribution and occurrence factors. *Landslides*, 16:765–776.

Zhao, B., Wang, Y., Li, W., Su, L., Lu, J., Zeng, L., and Li, X. (2021). Insights into the geohazards triggered by the 2017 Ms 6.9 Nyingchi earthquake in the east Himalayan syntaxis, China. *Catena*, 205:105467.

Zhao, C., Yang, W., Westoby, M., An, B., Wu, G., Wang, W., Wang, Z., Wang, Y., and Dunning, S. (2022). Brief communication: An approximately 50 $Mm^3$ ice-rock avalanche on 22 March 2021 in the Sedongpu valley, southeastern Tibetan Plateau. *The Cryosphere*, 16(4):1333–1340.